nature COMMUNICATIONS

ARTICLE

https://doi.org/10.1038/s41467-019-12889-w OPEN

A merged copper(I/II) cluster isolated from Glaser coupling

Siqi Zhang[1] & Liang Zhao[1*]

Ubiquitous copper-oxygen species are pivotal in enabling multifarious oxidation reactions in biological and chemical transformations. We herein construct a macrocycle-protected mixed-valence cluster [(^{t}BuC≡CCu$^I_3$)-(μ_2-OH)-Cu^{II}] by merging a copper acetylide cluster with a copper-oxygen moiety formed in Glaser coupling. This merged Cu(I/II) cluster shows remarkably strong oxidation capacity, whose reduction potential is among the most positive for Cu(II) and even comparable with some Cu(III) species. Consequently, the cluster exhibits high hydrogen atom transfer (HAT) reactivity with inert hydrocarbons. In contrast, the degraded [Cu^{II}-(μ_2-OH)-Cu^{II}] embedded in a small macrocyclic homologue shows no HAT reactivity. Theoretical calculations indicate that the strong oxidation ability of Cu(II) in [(^{t}BuC≡CCu$^I_3$)-(μ_2-OH)-Cu^{II}] is mainly ascribed to the uneven charge distribution of Cu(I) ions in the ^{t}BuC≡CCu$^I_3$ unit because of significant [$d_{Cu(I)} \rightarrow \pi^*_{(C\equiv C)}$] back donation. The present study on in situ formed metal clusters opens a broad prospect for mechanistic studies of Cu-based catalytic reactions.

[1] Key Laboratory of Bioorganic Phosphorus Chemistry & Chemical Biology (Ministry of Education), Department of Chemistry, Tsinghua University, Beijing 100084, China. *email: zhaolchem@mail.tsinghua.edu.cn

Copper–oxygen species are well-known in the active center of many enzymes[1–5] and organic synthetic transformations[6,7] to perform diversified oxidation reactions toward phenol[8], alcohol[9], amine[10], and even hydrocarbons[11]. In efforts to obtain fundamental chemical insights into their structures and reactivity, a number of important copper–oxygen complexes have been identified[12–18]. Comprehensive structure-property relationship studies on those copper–oxygen species have revealed that their reactivity is closely related to the oxidation capacity of copper centers. In this regard, many reported Cu(III)–oxygen species have been found possessing a powerful ability to activate inert C–H bonds by a hydrogen atom transfer (HAT) pathway[11,19,20] because the standard reduction potential of Cu(III)/Cu(II) (~1 V vs NHE) is more positive than that of Cu(II)/Cu(I) (0.15 V vs NHE)[21]. Nevertheless, high-valence copper centers are often difficult to isolate and sometimes the coordination adducts of Cu(III) are unstable under ambient conditions (e.g., Cu(III)–OH complex has to be studied at low temperature)[22]. Alternatively, subtle modulation of coordination environment of metal centers provides another avenue to achieve strong oxidative capacity[23]. For example, the Cu(II)/(I) reduction potentials of the blue copper sites in laccases vary from ~0.4 to ~0.8 V versus NHE by tuning the presence or absence of an axial methionine ligand[24]. In some particular cases of biomolecular systems such as particulate methane monoxygenase and multicopper oxidases, finely regulating the peripheral coordination environment of the copper–oxygen centers relies on additional nearby cluster aggregates, which effectively promote the oxidation capacity of the copper–oxygen sites and thus facilitate chemical transformations of inert molecules under mild conditions.

Glaser coupling reaction of terminal alkynes, one of the earliest known metal-catalyzed coupling reactions[25], has been extensively applied in the synthesis of conjugated diynes[26,27]. It is intriguingly featured by the use of low cost and relatively low toxicity Cu/O_2 reaction condition. Recent mechanistic studies have explored the activation of alkyne C–H bonds by a Cu(I)–Cu(II) synergistic process and substaniated the reduction of Cu(II) to Cu (I) through an oxidative coupling of acetylides[28,29]. However, as a key step of the catalytic cycle, the oxidation of Cu(I) to Cu(II) by oxygen in the presence of alkynes remains unclear up to now. The catalytic mechanism of the Glaser coupling reaction is closely related to both copper–oxygen species and copper-acetylide cluster moieties because the predominant σ- and π-bonding modes of acetylide facilitate the gathering of copper ions as reported in literatures[30,31]. The involvement of such two kinds of copper-based clusters makes the detailed oxidative step in the Glaser coupling reaction process very complicated. On the other hand, such Cu/O_2 environmentally benign reaction condition has also been applicable in numerous catalytic oxidative functionalization reactions of organic molecules[32]. It is expected that the isolation and characterization of organometallic copper/O_2 mixed-cluster intermediates would promote our understanding of catalytic mechanisms of the Cu/O_2-based organic transformations.

In this contribution, we report the isolation and characterization of the bi-cluster intermediate [(^{t}BuC≡CCu$^I_3$)-(μ_2-OH)-Cu^{II}] from the Glaser coupling reaction by using azacalix[8]pyridine (**Py[8]**) as a peripherally macrocyclic ligand (Fig. 1). This [(^{t}BuC≡CCu$^I_3$)-(μ_2-OH)-Cu^{II}] cluster in complex **1**, which can be regarded as merged from a [^{t}BuC≡CCu$_3$] and a [Cu-(μ_2-OH)-Cu] unit, features a remarkably strong oxidation capacity ($E_{1/2}$ = 0.77 V vs NHE)[33], among the most positive reduction potentials for Cu(II) so far[16–18,23,34,35]. Consequently, the [(^{t}BuC≡CCu$^I_3$)-(μ_2-OH)-Cu^{II}] cluster shows high reactivity in single-electron transfer (SET) and hydrogen atom transfer (HAT) reactions for various substrates including alcohol, amine, alkene and even inert alkane molecules with C(sp^3)–H bond dissociation energy (BDE) up to 99 kcal mol^{-1}. In contrast, the simple copper–oxygen species [Cu^{II}-(μ_2-OH)-Cu^{II}] in **2** isolated from the same Glaser coupling reaction mixture by a small macrocycle **Py[6]** exhibits no HAT reactivity due to the poor oxidative ability of Cu(II). Detailed characterizations and theoretical calculations indicate that the oxidation ability difference between [(^{t}BuC≡CCu$^I_3$)-(μ_2-OH)-Cu^{II}]@**Py[8]** and [Cu^{II}-(μ_2-OH)-Cu^{II}]@**Py[6]** (@ means encirclement) is mainly ascribed to the uneven positive charge distribution of Cu(I) in the ^{t}BuC≡CCu$^I_3$ unit due to significant [$d_{Cu(I)} \rightarrow \pi^*_{(C\equiv C)}$] back donation. Furthermore, the flexible conformation of **Py[8]** in **1** is propitious to stabilize the reduced Cu (I) products **3** and **4** derived from the SET and HAT reactions. Complex **4** can be further transformed to **3** by a deprotonated process.

Results

Synthesis and structural studies of clusters 1 and 2. Inspired by previous synthesis and oxidative reactivity studies of single metal–oxygen species (e.g., Fe(O) and Mn(O) species) stabilized by a size-matched macrocycle[36], we expect that macrocyclic compounds with large-sized cavity and flexible conformations may provide a convenient tool to access metal cluster units formed in the Glaser coupling reaction. Initially, the treatment of the polymeric [^{t}BuC≡CCu]$_n$ by [Cu(CH$_3$CN)$_4$](BF$_4$) and **Py[8]** generated a pale yellow suspension, which turned into maroon after introducing a certain amount of air into the mixture. The occurrence of Glaser coupling was confirmed by the detection of the homo-coupling product ^{t}BuC≡C-C≡C^{t}Bu in GC-MS (Supplementary Fig. 1). Diffusion of diethyl ether into the maroon solution deposited dark red crystals in a high yield of 75%. X-ray crystallographic analysis revealed the formula of this crystalline complex as [Cu$_4$(μ_3-^{t}BuC≡C)(μ_2-OH)(**Py[8]**)(CH$_3$CN)](BF$_4$)$_3$·2(CH$_3$OH)·2(H$_2$O) (**1**), wherein four copper ions are assigned as a Cu$^I_3$ + Cu^{II} combination based on the charge balance requirement and detailed structural characterizations vide infra. The mixed-valence Cu(I/II) species arises from the balance between the oxidation of Cu(I) to Cu(II) by oxygen and the reduction of Cu(II) to Cu(I) through an oxidative coupling process. Noteworthily, the synthetic yield of **1** is closely related to the stoichiometry of starting materials and the amount of injected air. After screening the stoichiometric ratio of **Py[8]**:^{t}BuC≡CCu:[Cu(CH$_3$CN)$_4$](BF$_4$), we found that the 1:5:10 ratio, rather than the 1:1:3 ratio shown in the formula, gave the highest yield. This can be rationalized by the fact that a portion of ^{t}BuC≡CCu^I and [Cu^{I}CH$_3$CN)$_4$](BF$_4$) have to be consumed by a certain amount of air to balance Cu(I/II) via the Glaser coupling (see Supplementary Data 1 for details).

As shown in the crystal structure of **1**, the cluster moiety within **Py[8]** can be regarded as from the fusion of an acetylide-centered trinuclear copper cluster with a [Cu-(μ_2-OH)-Cu] species by sharing a copper atom (Fig. 2a). The acetylide group C1≡C2 is bonded with three Cu(I) atoms via σ- (Cu1 and Cu2, 1.892(5)–1.973(5) Å) and π-type (Cu3, 1.994(5)–2.015(5) Å) coordination. Cu1 and Cu2 each is chelated by two adjacent pyridine rings while the acetonitrile-bonded Cu3 is connected with Cu4 by a μ_2-hydroxo. The relatively long bond distance of C1≡C2 (1.241(8) Å) plus the deviated bond angle of C1–C2–C3 (161.0(5)°) suggest a significant d(Cu3) → π*(C1≡C2) back donation. Furthermore, the biased bond lengths of Cu3–O1 (1.993(3) Å) and Cu4–O1 (1.858(3) Å) indicate different oxidation states of Cu3 and Cu4. Particularly, the Cu4–O1 distance is shorter than the Cu–O distances (1.87–1.93 Å) of many reported Cu(II)-(μ-OH) complexes[16–18,23,34,35]. These results together with the typical square planar coordination geometry support the 2 + charge state of Cu4.

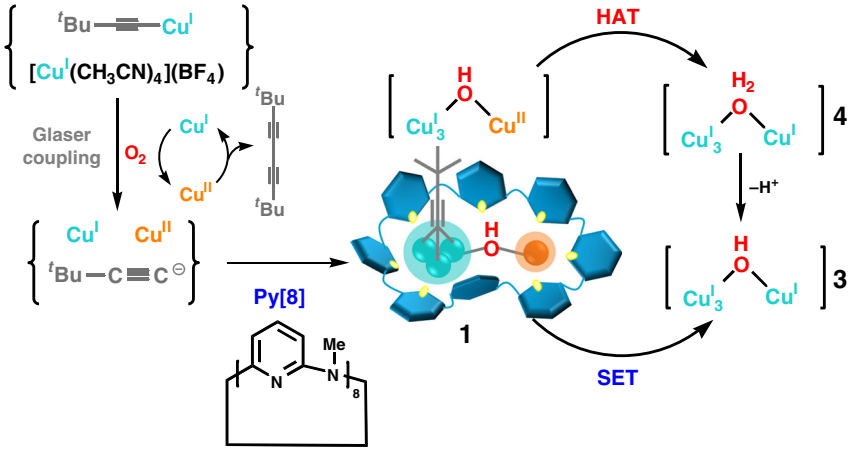

Fig. 1 Synthesis and transformations of complex **1**. Synthesis and transformations of the **Py[8]**-protected mixed-valence cluster [(^{t}BuC≡CCu$^I_3$)-(μ_2-OH)-Cu^{II}] in **1**

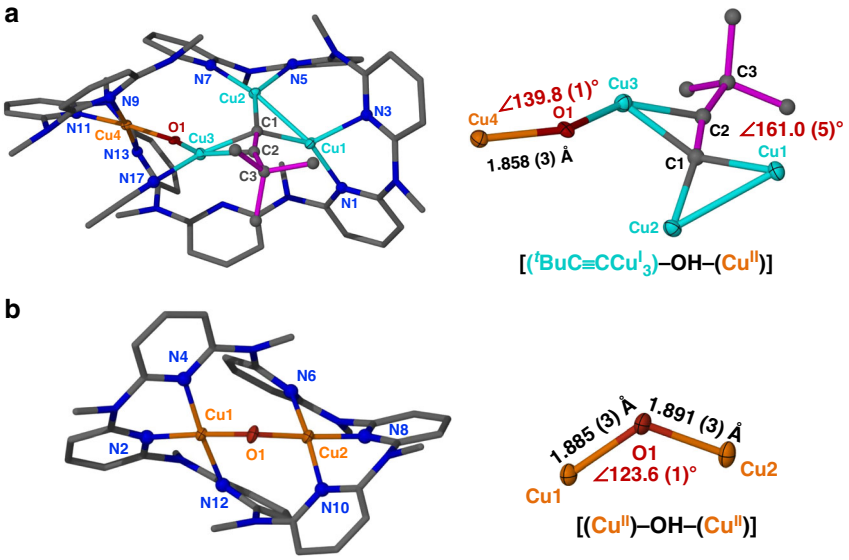

Fig. 2 Molecular structures of **1** and **2**. Crystal structures and the cluster cores of **a** complex **1** and **b** complex **2** with partial atom labeling (50% thermal ellipsoid probability level). Hydrogen atoms, BF_4^- anions, water and solvent molecules are omitted for clarity. Selected bond lengths and distances (Å) of **1**: C1–C2 1.241(8); C1–Cu1 1.973(5); C1–Cu2 1.892(5); C1–Cu3 1.994(5); C2–Cu3 2.015(5); Cu3–O1 1.993(3), Cu4–O1 1.858(3); Cu1–N1 1.988(4); Cu1–N3 2.111 (4); Cu2–N5 2.020(4); Cu2–N7 2.051(4); Cu3–N17 1.922(5); Cu4–N9 2.015(5); Cu4–N11 1.937(4); Cu4–N13 2.003(5); Cu1–Cu2 2.558(1). **2**: Cu1–O1 1.885 (3); Cu2–O1 1.891(3); Cu1–N2 1.932(3); Cu1–N4 1.979(3); Cu1–N12 2.050(3); Cu2–N6 2.039(3); Cu2–N8 1.931(3); Cu2–N10 1.989(3)

When a smaller macrocycle **Py[6]** in place of **Py[8]** was employed to trap the copper cluster species formed in the same Glaser coupling reaction mixture, purple crystals of **2** were deposited in a high yield of 67%. Due to the coordination restriction of **Py[6]**, only a [Cu^{II}-(μ_2-OH)-Cu^{II}] core is included in the crystal structure of **2** ([Cu$_2$(μ_2-OH)(**Py[6]**)(H_2O)$_{0.75}$](BF_4)$_3$·CH_3OH·H_2O) (Fig. 2b). This [Cu^{II}-(μ_2-OH)-Cu^{II}] core can be regarded as a fragment of the [(^{t}BuC≡CCu$^I_3$)-(μ_2-OH)-Cu^{II}] in **1**. Cu1 and Cu2 in **2** each is square-pyramidally chelated by three adjacent pyridine rings of **Py[6]**, a bridging hydroxo group and a remote water molecule. Therein, the bond lengths of Cu1–O1 (1.885(3) Å) and Cu2–O1 (1.891(3) Å) are comparable with Cu4–O1 in **1**, while the copper-water distances are in the range of 2.310(2)–2.406(1) Å.

The compositions of complexes **1** and **2** have been substantiated by elemental analysis for CHN and inductively coupled plasma optical emission spectrometer (ICP-OES) analysis for copper. Complexes **1** and **2** also kept their structure intact in solution as evidenced by electro-spray ionization mass spectroscopy (ESI-MS), electron paramagnetic resonance (EPR) and diffusion ordered spectroscopy (DOSY) experiment vide infra. The ESI-MS spectrum of **1** displayed three isotopically well-resolved peaks at m/z = 1374.2184, 643.6071, and 400.0702, which can be assigned to [Cu$^I_3$Cu^{II}(^{t}BuC≡C)(OH)(**Py[8]**)(BF_4)$_2$]$^+$, [Cu$^I_3$Cu^{II}(^{t}BuC≡C)(OH)(**Py[8]**)(BF_4)]$^{2+}$, and [Cu$^I_3$Cu^{II}(^{t}BuC≡C)(OH)(**Py[8]**)]$^{3+}$, respectively (Supplementary Fig. 2). Similarly, three isotopically well-resolved peaks at m/z = 953.1871, 433.0913, and 259.7266 corresponding to [Cu$^{II}_2$(OH)(**Py[6]**)(BF_4)$_2$]$^+$, [Cu$^{II}_2$(OH)(**Py[6]**)BF_4]$^{2+}$, and [Cu$^{II}_2$(OH)(**Py[6]**)]$^{3+}$, respectively, were also observed in the ESI-MS spectrum of **2** (Supplementary Fig. 3).

Other spectroscopic techniques were applied to gain further insights into the oxidation states of copper ions in complexes **1** and **2**. As shown in the electron paramagnetic resonance (EPR) spectra of **1**, the EPR signature for **1** in solid state was in good agreement with that in frozen-solution[37], confirming the consistency of

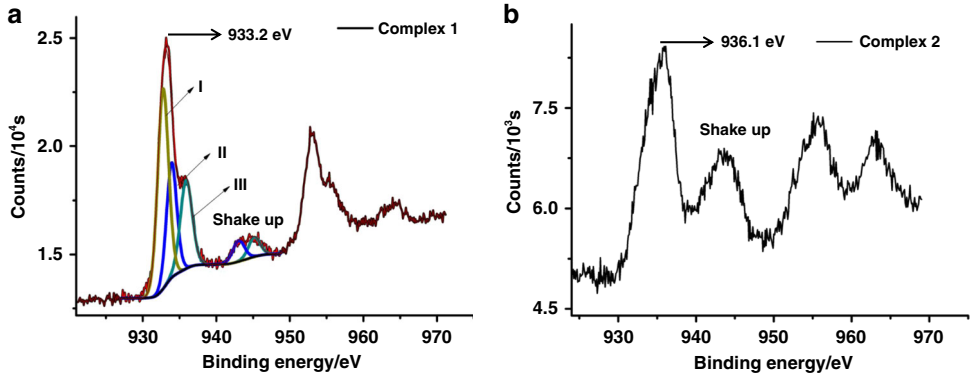

Fig. 3 XPS Characterizations. **a** XPS spectrum of **1** for Cu 2p (brown) with three fitting peaks **I–III** (Cu(I): yellow; Cu(I)′: blue; Cu(II): green). **b** XPS of **2** for Cu 2p signal

solid-state and solution structures (Supplementary Fig. 4 and Supplementary Data 2). The hyperfine coupling of $^{63/65}$Cu can be observed in the spectra of both crystal and powder samples of **1** (Supplementary Fig. 5), which should be ascribed to the long distance (~10 Å) and resulting weak spin-spin interactions between two Cu^{II}–Cu^{II} electronic spin centers. The characteristic g value relation of $g_{\parallel}$ ($g_z = 2.230$) > $g_{\perp}$ ($g_{x(y)} = 2.086$, $g_{y(x)} = 2.000$) supports the presence of Cu(II) in a square planar coordination geometry[38,39], which is in agreement with the crystal structure. Furthermore, quantitation of EPR active Cu(II) in the acetone solution of complex **1** based on a standard curve generated from Cu(II)-EDTA[40,41] confirmed the only existence of one Cu(II) in **1** (Supplementary Fig. 6). Besides, the existence of Cu(II) in **1** was also confirmed by the shake-up peak (Fig. 3a)[42] in X-ray photoelectron spectroscopy (XPS). In addition, XPS measurement further displayed an intensive peak at 933.2 eV for Cu 2p. In combination with the Auger electron spectroscopy (AES) of **1** that revealed a peak at 572.1 eV under X-ray irradiation of 1486.6 eV, the Auger parameter of this Cu 2p peak in **1** was then deduced to be 1847.7 eV (Supplementary Fig. 7). This is in good agreement with the standard CuCl sample (1847.6 eV)[43], showing the dominant presence of 1+ copper ions in **1**. Furthermore, the XPS spectrum of **1** can be nicely fitted by three sets of peaks **I**–**III** in a ratio of 2:1:1, which is consistent with the presence of two kinds of Cu(I) (Cu1/Cu2 and Cu3) and a Cu(II) (Cu4) in the crystal structure of **1**. Notably, the fitting Cu 2p energy for Cu3 (peak **II**, 934.1 eV) is higher than that of Cu1/Cu2 (peak **I**, 932.9 eV), implying the more positive nature of Cu3.

XPS measurement for **2** also showed an intensive peak of 936.1 eV for Cu 2p (Fig. 3b). The Auger parameter of this Cu 2p peak was then deduced as 1851.0 eV (Supplementary Fig. 8), which is in good agreement with the standard copper(II) oxide sample (1850.9 eV). These spectroscopic studies together with the shake-up peak in XPS confirm the presence of Cu(II) in **2**. The coupling mode between two hydroxo-bridged Cu(II) ions in **2** was subsequently explored by variable-temperature EPR studies. The EPR silent signatures (at $T = 5$ K) in acetone and in solid state (Supplementary Fig. 9) suggest an $S = 0$ ground spin state arising from the strong antiferromagnetic coupling of two Cu(II) mediated by a bridging hydroxo group[18]. Besides, magnetic susceptibility measurements on **2** by SQUID magnetometry result in an increase of $\chi_m T$ values along with the rising of the temperature (Supplementary Fig. 10), confirming an antiferromagnetic coupling system in complex **2**[44]. As complex **2** is EPR silent, DOSY experiment was then performed to demonstrate that the structure retains intact in solution. A single band with a diffusion coefficient $D = 8.393 \times 10^{-10}$ m^2 s^{-1} was observed in DOSY (Supplementary Fig. 11) and the diameter of this species was then deducted as 8.57 Å based on the Stokes–Einstein equation. This value agrees quite well with that in the crystal structure of **2** (9.06 Å).

Oxidation capacity studies of clusters 1 and 2. Cyclic voltammetry (CV) experiments were then performed to evaluate the oxidation capacity of **1** and **2**. CV of the deaerated acetone solution (0.1 M Bu_4NPF_6) of **1** (0.5 mM) revealed a quasi-reversible redox wave with $E_{1/2} = 0.14$ V vs Fc/Fc$^+$ (scan rate: 100 mV s^{-1}, Fig. 4a). This wave can be assigned as the 1e redox of Cu(II) to Cu(I) in the [(^{t}BuC≡CCu$^I_3$)-(OH)-Cu^{II}] of **1**, which was supported by the latter UV-vis titration experiment. Despite the only existence of low-valence Cu(I) and Cu(II) in **1**, to the best of our knowledge the Cu(II/I) reduction potential of [(^{t}BuC≡CCu$^I_3$)-(OH)-Cu^{II}] is more positive than most reported dinuclear copper(II)–oxygen complexes[16–18,23,34,35] and comparable with some copper(III)–oxygen species (Supplementary Data 3)[45–47]. The CV experiments of **1** have also been carried out with different scan rates (50–300 mV s^{-1}, Supplementary Fig. 12). The acquired curves gradually broadened along with the increasing of the scan rate and the ΔE values varied from 150 to 220 mV, suggesting a quasi-reversible redox system for complex **1**[48,49]. Such quasi-reversibility may result from the low electrochemical reaction rate of **1**, which is confirmed by the vide infra kinetic studies ($k_{et} = 2.19 \times 10^{-3}$ M^{-1} s^{-1}). In contrast, the CV measurement of **2** exhibited an irreversible wave with $E = -0.63$ V vs Fc/Fc$^+$ (scan rate: 100 mV s^{-1}, Fig. 4a), which is much negative compared with the reduction potential of complex **1**. The modulation of the scan rate (50–300 mV s^{-1}, Supplementary Fig. 13) did not change the irreversibility, suggesting the poor stability of the reduced form of **2**. In view of similar coordination environments provided by **Py[8]** in **1** and **Py[6]** in **2**, we conceive that the outstanding oxidation ability of **1** should be ascribed to the mixed-valence bi-cluster merged structure. The strong d→π* back donation from Cu3 to the acetylide group significantly increases the positive charge state of Cu3, which has been evidenced by above XPS studies. In addition, natural bond orbital (NBO) analyses in gas phase and in acetone both show that the natural charge on Cu3 is more positive than the other two copper(I) centers Cu1 and Cu2 (Fig. 5). Due to the presence of the nearby [^{t}BuC≡CCu$^I_3$] unit, the Cu4 center constitutes a remarkably short Cu–O bond with the bridging hydroxyl group, suggesting a high positive charge state of Cu4 as well. Consequently, the uneven charge distribution of copper ions in the [^{t}BuC≡CCu$^I_3$] cluster moiety and the remarkable positive nature of Cu3 and Cu4 both contribute to the oxidation capacity enhancement of the [(^{t}BuC≡C)Cu$^I_3$-(OH)-Cu^{II}] in **1**.

We next carried out the reduction of **1** by using a common organic reductant N,N,N′,N′-tetramethylphenylene-diamine (TMPD) to elucidate the redox process. When TMPD ($E_{ox} = -0.37$ V vs Fc/Fc$^+$) was mixed with **1** in acetone, a deep blue

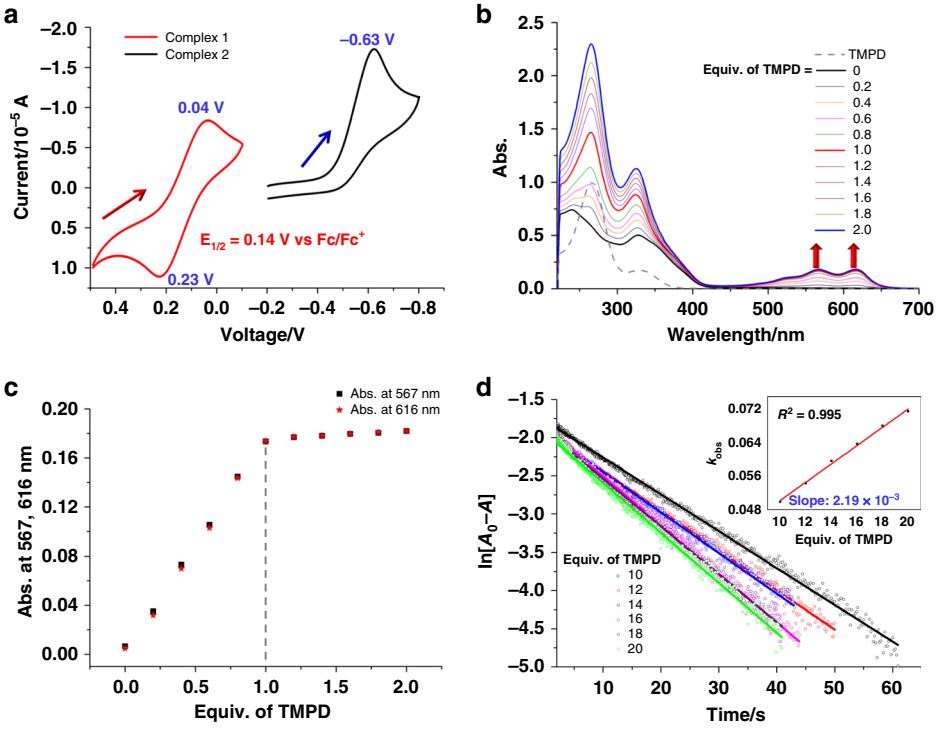

Fig. 4 CV, UV-vis titration and kinetic studies. **a** CV curves of **1** and **2** (0.5 mM) in deaerated acetone (0.1 M Bu_4NPF_6) at 298 K with a glassy carbon working electrode and a Ag/AgCl reference electrode. Scan rate: 100 mV s^{-1}. All potentials were measured against the Fc/Fc^+ redox couple. **b** Titration of **1** (0.6 mM) with TMPD monitored by UV-vis spectroscopy. **c** Characteristic absorbance at 567 and 616 nm upon adding different equivalents TMPD. **d** Pseudo-first-order plots of the TMPD-to-**1** electron transfer in acetone at 298 K. (Inset) Determination of k_{et} (298 K) by the plot of the pseudo-first-order rate constants (k_{obs}) versus the concentrations of TMPD

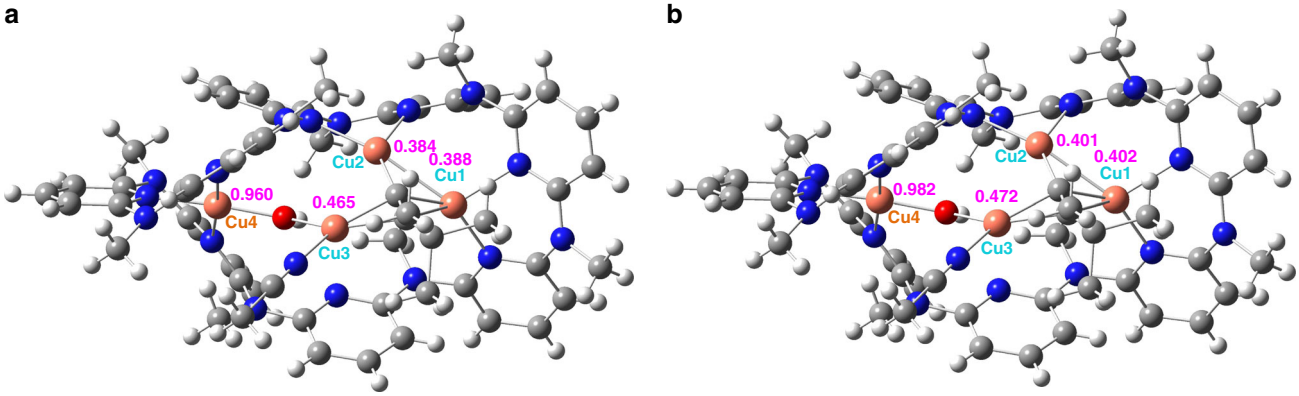

Fig. 5 NBO analyses for the charge distribution of metal ions in complex **1**. **a** NBO calculation in gas phase. **b** NBO calculation in acetone. Color codes: Cu, orange; N, blue; O, red; C, gray; H, light gray

solution with new absorption bands around 450–650 nm due to $TMPD^{\bullet+}$ was observed (Fig. 4b)[48,50,51]. A titration experiment monitored by UV-vis spectroscopy revealed saturated reduction by adding one equivalent TMPD (Fig. 4c), which is consistent with the 1e redox in the CV study. The stopped flow measurements were subsequently performed to determine the rate of SET at room temperature. As shown in Fig. 4d, the SET process of **1** obeyed pseudo-first-order kinetic. The second-order electron transfer rate constant (k_{et}) was consequently determined to be 2.19×10^{-3} M^{-1} s^{-1} based on the slope of linear plot of the pseudo-first order rate constants versus the concentrations of TMPD. In contrast, a reported mononuclear Cu(II) complex containing a flexible tridentate ligand has a faster SET rate constant (9.40 M^{-1} s^{-1}) upon reacting with TMPD[51]. The relatively slow k_{et} of **1** is consistent with the large ΔE value determined in the above-mentioned CV experiments. We conjecture that the slow k_{et} of **1** may arise from the rigid square planar coordination geometry of the Cu(II) center, which is hard to undergo prompt conformational adjustment in the redox process due to the presence of a neighboring ^{t}BuC≡CCu_3 cluster within the same **Py[8]**.

The strong oxidation capacity of **1** guarantees its high SET reactivity with extensive substrates under mild conditions. When 2,2,6,6-tetramethylpiperidine-1-oxyl (TEMPO), tetrahydrofuran (THF), isopropanol, and 4-aminophenol were applied to react with **1** in dichloromethane at room temperature, the characteristic absorption band of **1** at 326 nm, which was confirmed by theoretical calculation (Supplementary Fig. 14), gradually

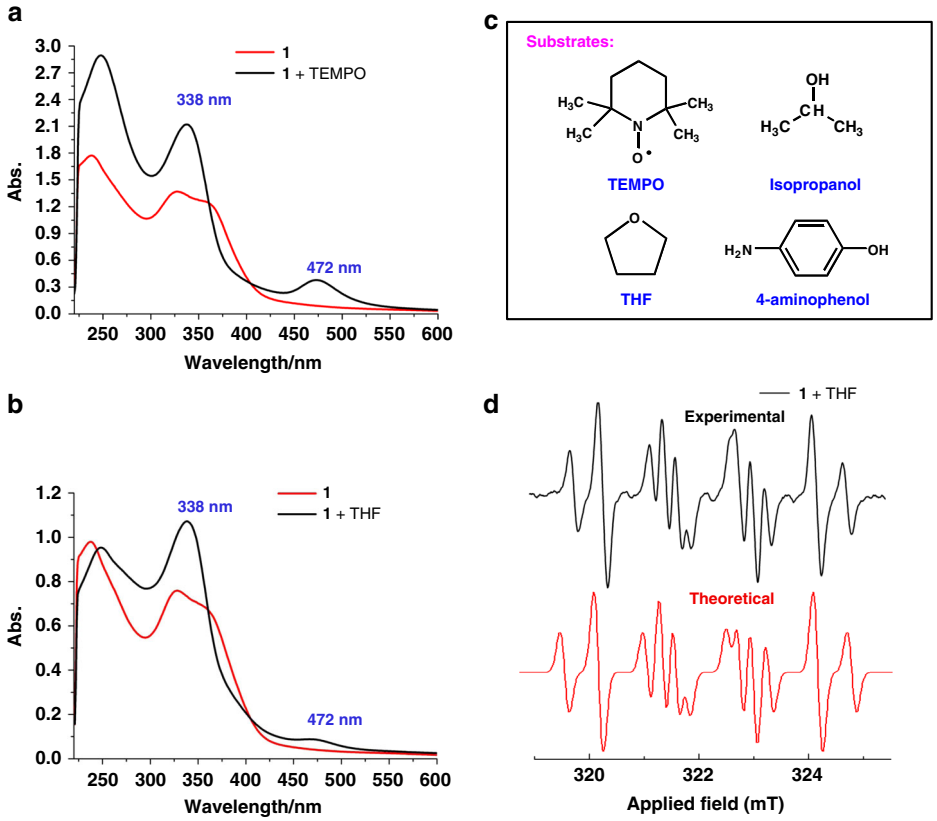

Fig. 6 SET studies of complex **1**. UV-vis spectra of reaction mixtures between **1** and **a** TEMPO, and **b** THF. **c** Organic substrates applicable for the SET reaction with **1**. **d** EPR measurement for capturing the radical product derived from the SET of THF with **1** in DMSO. 5,5-Dimethyl-1-pyrroline N-oxide was used as a radical trapper

diminished. Meanwhile, two new absorption peaks at 338 and 472 nm concomitantly appeared (Fig. 6a–c and Supplementary Fig. 15). The reduced product (denoted as complex **3**) corresponding to the absorptions at 338 and 472 nm was stable enough to be subjected to EPR and XPS analysis. Therein, the EPR silent signature together with the single peak at 932.6 eV for Cu 2p and the deduced Auger parameter of 1847.9 eV in XPS confirmed the only presence of Cu(I) in **3** (Supplementary Fig. 16). ESI-MS revealed an isotopically well-resolved peak at $m/z = 600.1052$ corresponding to $[Cu^{I}_4(^{t}BuC{\equiv}C)(OH)(\mathbf{Py[8]})]^{2+}$ (Supplementary Fig. 17). In addition, the product derived from the SET reaction of THF with **1** was captured and characterized as an organic $THF^{\bullet+}$ radical by EPR (Fig. 6d and Supplementary Data 4), substantiating the 1e reduction of the $[^{t}BuC{\equiv}CCu^{I}_3$-$(OH)$-$Cu^{II}]$ species in **1** to the $[^{t}BuC{\equiv}CCu^{I}_3$-$(OH)$-$Cu^{I}]$ in **3**.

Complex **2** can be reduced by TMPD in acetone at room temperature as well, producing a deeply colored blue solution as similar as **1**. However, other less reductive substrates such as THF and isopropanol show no SET reactivity with **2**. The titration experiment between **2** and TMPD monitored by UV-vis spectroscopy revealed that two equivalents TMPD were required to accomplish the reduction, suggesting a two-electron transfer process for the $[Cu^{II}$-$(\mu_2$-$OH)$-$Cu^{II}]$ cluster in **2**. The stopped flow measurements showed that the electron transfer process obeyed pseudo-first-order kinetic and thus the 3rd-order rate constants (k_{et}) was determined as $3.43 \times 10^{-5}\ M^{-2}\ s^{-1}$ based on the slope of linear plot of the pseudo-first-order rate constants versus square of the concentrations of TMPD (Supplementary Fig. 18). In view of the relatively rigid conformation of **Py[8]** in complex **1** that causes a low k_{et}, we conceive that the CV irreversibility and the slow electron transfer rate constant of $[Cu^{II}$-$(\mu_2$-$OH)$-$Cu^{II}]$@**Py[6]** in **2** are also ascribed to the conformational rigidity of **Py[6]** and the resulting difficulty to adapt to the structural distortion of copper ions upon the Cu(II)-to-Cu(I) reduction. Further titration experiments monitored by ^{1}H-NMR were performed to identify the final products after the reaction of complex **2** with TMPD. Therein, a new set of peaks with the ratio of 1:2:3 gradually appear and increase along with the addition of TMPD (Supplementary Fig. 19). Further comparison with the NMR spectra of the neat **Py[6]** and metal-azacalixpyridine coordination adducts[52] revealed that the reduced product of complex **2** is a mixture of **Py[6]**-Cu^{I} adducts and some free copper(I) ions.

Hydrogen atom transfer studies of cluster 1. In view of strong oxidation capacity of high-valence metal–oxygen species of Mn, Fe, and Cu that are capable of enabling the activation of inert C–H bonds under mild conditions[53,54], we then conducted further reaction studies of **1** with hydrocarbons. Taken dihydroanthracene (DHA, bond dissociation energy (BDE) = 76 kcal mol^{-1})[55] as an example, the reaction of **1** with DHA at room temperature indeed generated the HAT product anthracene as evidenced in mass spectrum (Supplementary Fig. 20). Meanwhile, the $[(^{t}BuC{\equiv}C)Cu^{I}_3$-$(OH)$-$Cu^{II}]$ cluster abstracted a hydrogen atom to produce complex **4**, which is EPR silent and shows an characteristic absorption peak at 358 nm (Fig. 7a). Molecular formula of **4** was identified as $[Cu^{I}_4(^{t}BuC{\equiv}C)(H_2O)(\mathbf{Py[8]})](BF_4)_3$ based on ESI-MS, which showed three isotopically well-resolved peaks at $m/z = 1375.2201$, 644.1060, and 400.4049 corresponding to $[\mathbf{4}$-$(BF_4)]^{+}$, $[\mathbf{4}$-$2(BF_4)]^{2+}$, and $[\mathbf{4}$-$3(BF_4)]^{3+}$, respectively (Supplementary Fig. 21). By monitoring the characteristic 358 nm

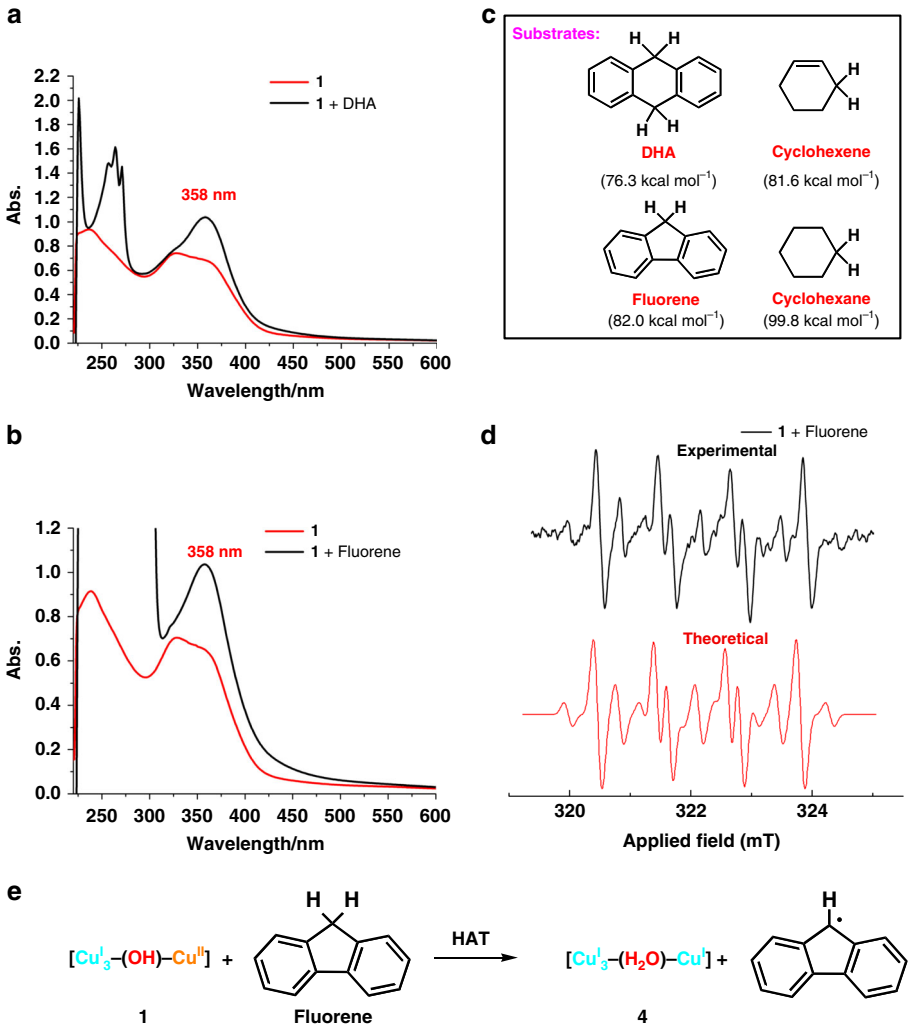

Fig. 7 HAT studies of complex **1**. UV-vis spectra of **1** and the products after reacting with **a** DHA and **b** fluorene. **c** HAT substrates with different BDEs. **d** EPR measurement for capturing the radical products in the reaction between fluorene and **1** in DMSO. 5,5-Dimethyl-1-pyrroline N-oxide was used as a radical trapper. **e** The alkyl radical generation process between **1** and fluorene

absorption band of **4**, we screened the scope of substrates for the HAT reaction with **1**. Several hydrocarbon substrates (e.g., fluorene, cyclohexene, and cyclohexane) with BDE[55] up to 99 kcal mol^{-1} were found reacting with complex **1** via a HAT reaction pathway (Fig. 7b, c and Supplementary Fig. 22). Particularly, the newly generated radical species arising from the reaction of fluorene with **1** were identified by EPR (Fig. 7d, e and Supplementary Data 4). The theoretical simulation shows the presence of the predominant fluorene-based alkyl radicals together with a small amount of hydroxyl radicals in the reaction mixture of **1** and fluorene. The latter hydroxyl radicals may result from the reaction of **1** with a little H_2O in the system. In contrast, no HAT reaction was observed between complex **2** and DHA or other hydrocarbons (Supplementary Fig. 23). Besides the **1**-to-**3** and **1**-to-**4** transformations relying on SET and HAT, respectively, we found that complex **4** can be deprotonated by a strong base 1,8-diazabicyclo[5.4.0]undec-7-ene (DBU) to generate **3**. As shown in the UV-vis titration, there is an isobestic point at 450 nm between 358 (the typical absorption of **4**) and 472 nm (the absorption of **3**), suggesting the occurrence of a clean and uniform **4**-to-**3** transformation (Supplementary Fig. 24). The isolation and interconversion of three intermediate species **1**, **3**, and **4** should be attributed to the extraordinarily protective role of the macrocycle **Py[8]**[56,57].

Discussion

Although a number of Cu/O_2-involved catalytic oxidative functionalization reactions of organic molecules have been reported to date, however, most of the proposed organometallic copper–oxygen intermediates have yet to be trapped and characterized[32]. In this work, two different copper–oxygen species [(^{t}BuC≡CCu$^I_3$)-(μ_2-OH)-Cu^{II}] in **1** and [Cu^{II}-(μ_2-OH)-Cu^{II}] in **2** are in situ isolated from the same Glaser coupling reaction system by using differently sized macrocyclic ligands. The [Cu^{II}-(μ_2-OH)-Cu^{II}] encapsulated in a small macrocycle **Py[6]** can be regarded as a fragment species of the [(^{t}BuC≡CCu$^I_3$)-(μ_2-OH)-Cu^{II}] in a relatively large macrocycle **Py[8]**. While such two copper–oxygen clusters have similar coordination environments due to the peripheral polypyridine homologs **Py[6]** and **Py[8]**, they show distinct oxidative capacity and reactivity. The strong oxidation capacity of the copper(II)–oxygen species in [(^{t}BuC≡CCu$^I_3$)-(μ_2-OH)-Cu^{II}] is comparative with some binuclear copper(III)–oxygen species for C–H activation. Such remarkable oxidation ability of the Cu(II) center in [(^{t}BuC≡CCu$^I_3$)-(μ_2-OH)-Cu^{II}] have been attributed to the presence of a nearby ^{t}BuC≡CCu$^I_3$ cluster within the same macrocycle. Therein, the significant d(Cu)-π*(C≡C) back donation plus the high electronegativity of sp-hybridized carbon center play a very important role. In addition, although the formal charge of the [^{t}BuC≡CCu$^I_3$] moiety equals to a 2+ charged metal ion, the

dipolar effect due to the spatial arrangement of three Cu(I) ions in ^{t}BuC≡CCu$^{I}_3$ may also affect the oxidation ability of the adjacent copper(II)–oxygen species. Furthermore, the structural flexibility of the large macrocycle **Py[8]** makes it adapt to the coordination geometries of different valence metal ions and finally accounts for the isolation of SET and HAT products **3** and **4**. In this sense, the present work illustrates the excellent capability and high efficiency of large polydentate macrocycles in the stabilization and isolation of polynuclear reactive intermediates that are in situ formed in reaction mixtures. The trap of structurally correlated intermediate species by differently sized macrocycles is conducive to identify true catalytic species by stitching the acquired fragments.

On the other hand, the identification of different reactive intermediates provides comprehensive perspectives to understand detailed reaction mechanisms. To the best of our knowledge, the mixed-valence cluster [(^{t}BuC≡CCu$^{I}_3$)-(μ$_2$-OH)-Cu^{II}] represents the first bi-cluster intermediate structure directly trapped from the Glaser coupling reaction mixture. CV studies on [(^{t}BuC≡C-Cu$^{I}_3$)-(μ$_2$-OH)-Cu^{II}]@**Py[8]** and the degraded species [Cu^{II}-(μ$_2$-OH)-Cu^{II}]@**Py[6]** have shown that the Cu(II/I) reduction potential of the former is more positive (~0.8 V) than the latter. As a consequence, the [(^{t}BuC≡CCu$^{I}_3$)-(μ$_2$-OH)-Cu^{II}]@**Py[8]** species shows high SET and HAT reactivity with substrates in a broad scope while the [Cu^{II}-(OH)-Cu^{II}]@**Py[6]** only undergoes a SET reaction pathway with strong reducing agents (e.g., TMPD). Particularly, the [(^{t}BuC≡CCu$^{I}_3$)-(μ$_2$-OH)-Cu^{II}]@**Py[8]** exhibits HAT reactivity with hydrocarbons with C(sp^3)–H bond dissociation energy up to 99 kcal mol^{-1} like other high-valent Mn (IV and V), Fe(IV), and Cu(III) oxygen species[58]. Compared with the common [Cu^{II}-(OH)-Cu^{II}] species that is often considered as catalytic species in Cu/O$_2$-based organic transformations, the remarkable oxidation ability and high reactivity of the bi-cluster intermediate [(^{t}BuC≡CCu$^{I}_3$)-(μ$_2$-OH)-Cu^{II}] implies that the in situ formed organometallic/copper–oxygen merged clusters may serve as the true catalytic species in both Glaser coupling reaction and other Cu/O$_2$-catalyzed organic transformations. The present study on the remarkably oxidative bi-cluster intermediate sheds light on the mechanistic study of Glaser coupling and other copper-catalyzed reactions of alkynes, and is conducive to rationally promote the activity of copper catalysts in the future.

In conclusion, we have successfully isolated two in situ copper–oxygen intermediates [(^{t}BuC≡CCu$^{I}_3$)-(μ$_2$-OH)-Cu^{II}] and [Cu^{II}-(μ$_2$-OH)-Cu^{II}] from the Glaser coupling reaction mixture by using size-tunable macrocycles. The remarkable oxidation capacity and the resulting high SET and HAT reactivity of [^{t}BuC≡CCu$^{I}_3$-(μ$_2$-OH)-Cu^{II}]@**Py[8]** have been ascribed to its unique bi-cluster structure based on detailed characterizations, theoretical calculations and the comparison with the [Cu^{II}-(μ$_2$-OH)-Cu^{II}]@**Py[6]** cluster. The obtaining of the bi-cluster merged structure expands the library of copper–oxygen species and sheds light on the mechanistic study of Glaser coupling. Unveiling the high reactivity of in situ formed organometallic clusters also broadens our horizons on the development of highly efficient metal catalysts in the future studies.

Methods

General information. All commercially available chemicals were used without further purification. The solvents used in this study were processed by standard procedures. ^{1}H-NMR experiments were carried out on a JEOL ECX-400 MHz instrument. DOSY experiment was carried out on a Bruker Avance 600 MHz instrument using a 5 mm TXI H-C/N-D Z-GRD probe. 2D sequence for diffusion measurements were conducted using stimulated echo with 1 spoil gradient. Mass spectra were obtained using a Thermo Scientific Exactive Orbitrap instrument. UV-vis measurements were performed using Agilent Cary Series UV-Vis-NIR. EPR experiments were carried out using JEOL JES-FA200 ESR Spectrometer and Bruker E580. Elemental analyses were recorded on a Thermo FlashEA 1112 elemental analyzer. The details of X-ray crystallographic measurements are summarized in Supplementary Data 5 and 6.

Synthesis of macrocyclic ligands Py[8] and Py[6]. Macrocyclic ligands **Py[8]** and **Py[6]** were prepared according to the published method by the Pd-catalyzed fragment coupling protocol[59,60]. Starting with 2,6-dibromopyridine and methylamine, reiterative aromatic nucleophilic substitution reactions afforded α,ω-dibrominated and α,ω-diaminated linear oligomers (NaH, THF, reflux). **Py[8]** was synthesized by macrocyclic cross coupling reaction between α,ω-dibrominated linear pentamer (661 mg, 1.1 mmol) and α,ω-diaminated linear trimer (349 mg, 1.0 mmol) using Pd$_2$(dba)$_3$ (138 mg, 0.15 mmol), dppp (124 mg, 0.3 mmol) and NaO^{t}Bu (288 mg, 3 mmol) in toluene (400 mL, reflux) under nitrogen protection. **Py[6]** was synthesized under the same reaction condition by macrocyclic cross coupling reaction between α,ω-dibrominated linear trimer (494 mg, 1.1 mmol) and α,ω-diaminated linear trimer (349 mg, 1.0 mmol).

Synthesis of complex 1. Under nitrogen protection, **Py[8]** (8.5 mg, 0.01 mmol), [Cu(CH$_3$CN)$_4$](BF$_4$) (31.4 mg, 0.1 mmol), and [^{t}BuC≡CCu] (7.3 mg, 0.05 mmol) were dissolved in a mixed solvent of anhydrous methanol and dichloromethane (1.5 mL, v/v = 1/1) in a 10 mL Schlenk tube. After stirred for half an hour at room temperature, air (3 mL) was injected to the system via syringe. The mixture was further stirred for 3 h and the solution color changed from light yellow to maroon. After filtration, the filtrate was diffused by diethyl ether to obtain dark red crystals of **1** (12.1 mg, 75% yield). Elemental analysis for **1**·(H$_2$O)·(CH$_2$Cl$_2$)$_2$: C$_{58}$H$_{67}$B$_3$Cl$_4$Cu$_4$F$_{12}$N$_{17}$O$_2$ (after remove solvent under vacuum), found (calcd): C 41.32 (41.20); H 3.94 (3.99); N 14.29 (14.08). Content of copper for **1** determined by ICP-OES (found (calcd) in wt%): 16.92 (16.91). High-resolution ESI-MS: m/z = 1374.2184, 643.6071, and 400.0702 corresponding to [Cu$^{I}_3$Cu^{II}(^{t}BuC≡C)(OH)(**Py[8]**)(BF$_4$)$_2$]$^+$, [Cu$^{I}_3$Cu^{II}(^{t}BuC≡C)(OH)(**Py[8]**)(BF$_4$)]$^{2+}$, and [Cu$^{I}_3$Cu^{II} (^{t}BuC≡C)(OH)(**Py[8]**)]$^{3+}$, respectively.

Synthesis of complex 2. The synthetic procedure for **2** was similar to that of **1** but using **Py[6]** in place of **Py[8]**. Purple crystals of **2** were obtained in 67% yield (7.2 mg) by three-day evaporation. Elemental analysis for **2**·(H$_2$O)·(CH$_2$Cl$_2$): C$_{37}$H$_{41}$B$_3$Cl$_2$Cu$_2$F$_{12}$N$_{12}$O$_2$ (after remove solvent under vacuum), found (calcd) in C 39.25 (38.84); H 3.62 (3.61); N 14.77 (14.69). Content of copper for **2** determined by ICP-OES (found (calcd) in wt%): 12.86 (12.21). High-resolution ESI-MS: m/z = 953.18707, 433.09131, and 259.72665 corresponding to [Cu$^{II}_2$(OH)(Py[6])(BF$_4$)$_2$]$^+$, [Cu$^{II}_2$(OH)(Py[6])BF$_4$]$^{2+}$, and [Cu$^{II}_2$(OH)(Py[6])]$^{3+}$, respectively.

Computational details. Theoretical calculation of **1** was performed using the Gaussian 09 program[61]. Initial structure for natural bond orbital (NBO) analysis of **1** for calculation was built up on the basis of single-crystal structure. Structure **1′** for optimization was also built up on the basis of single-crystal structure but methyl groups bonded to the bridged nitrogen atoms in the macrocyclic ligand **Py[8]** were replaced by hydrogen atoms for clarity (Supplementary Data 7). Becke three-parameter hybrid functional accompanied by Lee–Yang–Parr correlation functional (B3LYP)[62,63] were employed in DFT calculation without any symmetry constraints on molecular structures. Dunning correlation-consistent basis set cc-pVTZ-pp (a triple-ζ basis set)[64,65] were applied for copper atoms and 6-311G** basis set[66] for other atoms in NBO calculation. The Hay and Wadt effective core potentials with a double-ζ basis set (LanL2DZ)[67–70] were applied for copper atoms and 6-31G basis set[66] for other atoms in optimization for molecular orbitals. The root is set as 1 in all of the DFT calculations.

Data availability

The X-ray crystallographic coordinates for structures reported in this work have been deposited at the Cambridge Crystallographic Data Center (CCDC), under deposition number CCDC-1867699 (complex **1**), and CCDC-1880841 (complex **2**). These data can be obtained free of charge from the Cambridge Crystallographic Data Centre via www.ccdc.cam.ac.uk/data_request/cif. For full characterization data including UV-vis spectra, High-resolution ESI-MS, EPR, XPS, SQUID, NMR, CV, DFT calculations and experimental details, see the Supplementary Information and Supplementary Data. Any further relevant data are available from the authors upon reasonable request.

Received: 21 March 2019; Accepted: 8 October 2019;
Published online: 24 October 2019

References

1. Lieberman, R. L. & Rosenzweig, A. C. Crystal structure of a membrane-bound metalloenzyme that catalyses the biological oxidation of methane. *Nature* **434**, 177–182 (2005).
2. Cao, L., Caldararu, O., Rosenzweig, A. C. & Ryde, U. Quantum refinement does not support dinuclear copper sites in crystal structures of particulate methane monooxygenase. *Angew. Chem. Int. Ed.* **57**, 162–166 (2018).
3. Solomon, E. I., Sundaram, U. M. & Machonkin, T. E. Multicopper oxidases and oxygenases. *Chem. Rev.* **96**, 2563–2605 (1996).

4. Quintanar, L. et al. Spectroscopic and electronic structure studies of the trinuclear Cu cluster active site of the multicopper oxidase laccase: nature of its coordination unsaturation. *J. Am. Chem. Soc.* **127**, 13832–13845 (2005).
5. Yoon, J., Fujii, S. & Solomon, E. I. Geometric and electronic structure differences between the type 3 copper sites of the multicopper oxidases and hemocyanin/tyrosinase. *Proc. Natl Acad. Sci. USA* **106**, 6585–6590 (2009).
6. Tang, X., Wu, W., Zeng, W. & Jiang, H. Copper-catalyzed oxidative carbon-carbon and/or carbon-heteroatom bond formation with O_2 or internal oxidants. *Acc. Chem. Res.* **51**, 1092–1105 (2018).
7. Campbell, A. N. & Stahl, S. S. Overcoming the "oxidant problem": strategies to use O_2 as the oxidant in organometallic C-H oxidation reactions catalyzed by Pd (and Cu). *Acc. Chem. Res.* **45**, 851–863 (2012).
8. Chiang, L., Keown, W., Citek, C., Wasinger, E. C. & Stack, T. D. P. Simplest monodentate imidazole stabilization of the oxy-tyrosinase Cu_2O_2 core: phenolate hydroxylation through a Cu^{III} intermediate. *Angew. Chem. Int. Ed.* **55**, 10453–10457 (2016).
9. McCann, S. D., Lumb, J.-P., Arndtsen, B. A. & Stahl, S. S. Second-order biomimicry: in situ oxidative self-processing converts copper(I)/diamine precursor into a highly active aerobic oxidation catalyst. *ACS Cent. Sci.* **3**, 314–321 (2017).
10. Kim, S. et al. Amine oxidative N-dealkylation via cupric hydroperoxide Cu-OOH homolytic cleavage followed by site-specific fenton chemistry. *J. Am. Chem. Soc.* **137**, 2867–2874 (2015).
11. Dhar, D. & Tolman, W. B. Hydrogen atom abstraction from hydrocarbons by a copper(III)-hydroxide complex. *J. Am. Chem. Soc.* **137**, 1322–1329 (2015).
12. Fukuzumi, S. & Karlin, K. D. Kinetics and thermodynamics of formation and electron-transfer reacions of Cu–O_2 and Cu_2–O_2 complexes. *Coord. Chem. Rev.* **257**, 187–195 (2013).
13. Chen, P. P.-Y., Nagababu, P., Yu, S. S.-F. & Chan, S. I. Development of the tricopper cluster as a catalyst for the efficient conversion of methane into MeOH. *ChemCatChem* **6**, 429–437 (2014).
14. Haack, P. & Limberg, C. Molecular Cu^{II}-O-Cu^{II} complexes: still waters run deep. *Angew. Chem. Int. Ed.* **53**, 4282–4293 (2014).
15. Wang, V. C.-C. et al. Alkane oxidation: methane monooxygenases, related enzymes, and their biomimetics. *Chem. Rev.* **117**, 8574–8621 (2017).
16. Ali, G., VanNatta, P. E., Ramirez, D. A., Light, K. M. & Kieber-Emmons, M. T. Thermodynamics of a μ-oxo dicopper(II) complex for hydrogen atom abstraction. *J. Am. Chem. Soc.* **139**, 18448–18451 (2017).
17. Garcia-Bosch, I. et al. Dioxygen activation by a macrocyclic copper complex leads to a Cu_2O_2 core with unexpected structure and reactivity. *Chem. Eur. J.* **22**, 5133–5137 (2016).
18. Haack, P. et al. Access to a Cu^{II}-O-Cu^{II} motif: spectroscopic properties, solution structure, and reactivity. *J. Am. Chem. Soc.* **135**, 16148–16160 (2013).
19. Citek, C., Lin, B.-L., Phelps, T. E., Wasinger, E. C. & Stack, T. D. P. Primary amine stabilization of a dicopper(III) bis(μ-oxo) species: modeling the ligation in pMMO. *J. Am. Chem. Soc.* **136**, 14405–14408 (2014).
20. Citek, C., Herres-Pawlis, S. & Stack, T. D. P. Low temperature syntheses and reactivity of Cu_2O_2 active-site models. *Acc. Chem. Res.* **48**, 2424–2433 (2015).
21. Keown, W., Gary, J. B. & Stack, T. D. P. High-valent copper in biomimetic and biological oxidations. *J. Biol. Inorg. Chem.* **22**, 289–305 (2017).
22. Donoghue, P. J. et al. Rapid C-H bond activation by a monocopper(III)-hydroxide complex. *J. Am. Chem. Soc.* **133**, 17602–17605 (2011).
23. Bansal, D. & Gupta, R. Hydroxide-bridged dicopper complexes: the influence of secondary coordination sphere on structure and catecholase activity. *Dalton. Trans.* **46**, 4617–4627 (2017).
24. Jones, S. M. & Solomon, E. I. Electron transfer and reaction mechanism of laccases. *Cell. Mol. Life Sci.* **72**, 869–883 (2015).
25. Hay, A. S. Oxidative coupling of acetylenes. II1. *J. Org. Chem.* **27**, 3320–3321 (1962).
26. Siemsen, P., Livingston, R. C. & Diederich, F. Acetylenic coupling: a powerful tool in molecular construction. *Angew. Chem. Int. Ed.* **39**, 2632–22657 (2000).
27. Leophairatana, P., Samanta, S., Silva, C. C. D. & Koberstein, J. T. Preventing alkyne-alkyne (i.e., Glaser) coupling associated with the ATRP synthesis of alkyne-functional polymers/macromonomers and for alkynes under click (i.e., CuAAC) reaction conditions. *J. Am. Chem. Soc.* **139**, 3756–3766 (2017).
28. Zhang, G. et al. Direct observation of reduction of Cu(II) to Cu(I) by terminal alkynes. *J. Am. Chem. Soc.* **136**, 924–926 (2014).
29. Bai, R. et al. Cu(II)-Cu(I) synergistic cooperation to lead the alkyne C-H activation. *J. Am. Chem. Soc.* **136**, 16760–16763 (2014).
30. Berg, R. & Straub, B. F. Advancements in the mechanistic understanding of the copper-catalyzed azide–alkyne cycloaddition. *Beilstein J. Org. Chem.* **9**, 2715–2750 (2013).
31. Bruce, M. I. et al. Structural systematics of some trinuclear alkynyl and diynyl Group 11 complexes containing dppm [dppm = $CH_2(PPh_2)_2$]. *Coord. Chem. Rev.* **375**, 2–12 (2018).
32. Trammell, R., Rajabimoghadam, K. & Garcia-Bosch, I. Copper-promoted functionalization of organic molecules: from biologically relevant Cu/O_2 model systems to organometallic transformations. *Chem. Rev.* **119**, 2954–3031 (2019).
33. Pavlishchuk, V. V. & Addison, A. W. Conversion constants for redox potentials measured versus different reference electrodes in acetonitrile solutions at 25 °C. *Inorg. Chim. Acta* **298**, 97–102 (2000).
34. Mandal, S., Mukherjee, J., Lloret, F. & Mukherjee, R. Modeling tyrosinase and catecholase activity using new m-xylyl-based ligands with bidentate alkylamine terminal coordination. *Inorg. Chem.* **51**, 13148–13161 (2012).
35. Fukuzumi, S. et al. Factors that control catalytic two- versus four-electron reduction of dioxygen by copper complexes. *J. Am. Chem. Soc.* **134**, 7025–7035 (2012).
36. Baglia, R. A., Zaragoza, J. P. T. & Goldberg, D. P. Biomimetic reactivity of oxygen-derived manganese and iron porphyrinoid complexes. *Chem. Rev.* **117**, 13320–13352 (2017).
37. Wagner, C. L. et al. Dispersion-force-assisted disproportionation: a stable two-coordinate copper(II) complex. *Angew. Chem. Int. Ed.* **55**, 10444–10447 (2016).
38. Nellutla, S. et al. Magnetism, electron paramagnetic resonance, electrochemistry, and mass spectrometry of the pentacopper(II)-substituted tungstosilicate $[Cu_5(OH)_4(H_2O)_2(A\text{-}\alpha\text{-}SiW_9O_{33})_2]^{10-}$, a model five-spin frustrated cluster. *Inorg. Chem.* **44**, 9795–9806 (2005).
39. Garribba, E. & Micera, G. The Determination of the geometry of Cu(II) complexes an EPR spectroscopy experiment. *J. Chem. Educ.* **83**, 1229–1232 (2006).
40. Smith, S. M. et al. Crystal structure and characterization of particulate methane monooxygenase from *Methylocystis* species strain M. *Biochemistry* **50**, 10231–10240 (2011).
41. Tao, L. et al. Copper binding sites in the manganese-oxidizing Mnx protein complex investigated by electron paramagnetic resonance spectroscopy. *J. Am. Chem. Soc.* **139**, 8868–8877 (2017).
42. Brigs, D. & Seah, M. P. (eds.). *Practical Surface Analysis by Auger and X-ray Photoelectron Spectroscopy*. (Wiley, New York, 1983).
43. Moulder, J. F., Stickle, W. F., Sobol, P. E. & Bomben, K. D. in *Handbook of X-ray Photoelectron Spectroscopy* (eds Chastain, J. & King, R. C.) (Physical Electronics, Minnesota, 1992).
44. Nikolayenko, V. I. et al. Inclusion of a dithiadiazolyl radical in a seemingly non-porous solid. *Chem. Commun.* **53**, 11310–11313 (2017).
45. Cole, A. P., Mahadevan, V., Mirica, L. M., Ottenwaelder, X. & Stack, T. D. P. Bis(μ-oxo)dicopper(III) complexes of a homologous series of simple peralkylated 1,2-diamines: steric modulation of structure, stability, and reactivity. *Inorg. Chem.* **44**, 7345–7364 (2005).
46. Lionetti, D., Day, M. W. & Agapie, T. Metal-templated ligand architectures for trinuclear chemistry: tricopper complexes and their O_2 reactivity. *Chem. Sci.* **4**, 785–790 (2013).
47. Dhar, D. et al. Perturbing the copper(III)-hydroxide unit through ligand structural variation. *J. Am. Chem. Soc.* **138**, 356–368 (2016).
48. Tahsini, L. et al. Electron-transfer reduction of dinuclear copper peroxo and bis-μ-oxo complexes leading to the catalytic four-electron reduction of dioxygen to water. *Chem. Eur. J.* **18**, 1084–1093 (2012).
49. Neisen, B. D., Solntsev, P. V., Halvagar, M. R. & Tolman, W. B. Secondary sphere hydrogen bonding in monocopper complexes of potentially dinucleating bis(carboxamide) ligands. *Eur. J. Inorg. Chem.* **2015**, 5856–5863 (2015).
50. Rosokha, S. V. & Kochi, J. K. Continuum of outer- and inner-sphere mechanisms for organic electron transfer. steric modulation of the precursor complex in paramagnetic (ion-radical) self-exchanges. *J. Am. Chem. Soc.* **129**, 3683–3697 (2007).
51. Tano, T. et al. Redox properties of a mononuclear copper(II)-superoxide complex. *Inorg. Chem.* **52**, 10431–10437 (2013).
52. He, X. et al. Synthesis of stable polymetalated aromatic complexes through metal-macrocycle capsule-triggered cyclization. *Chem. Sci.* **9**, 1481–1487 (2018).
53. Mayer, J. M. Understanding hydrogen atom transfer: from bond strengths to Marcus theory. *Acc. Chem. Res.* **44**, 36–46 (2011).
54. Warren, J. J., Tronic, T. A. & Mayer, J. M. Thermochemistry of proton-coupled electron transfer reagents and its implications. *Chem. Rev.* **110**, 6961–7001 (2011).
55. Luo, Y. (ed.). *Handbook of Bond Dissociation Energies in Organic Compounds* (pp. 11–93. CRC Press, New York, 2002).
56. Raynal, M., Ballester, P., Vidal-Ferran, A. & van Leeuwen, P. W. N. M. Supramolecular catalysis. Part 2: artificial enzyme mimics. *Chem. Soc. Rev.* **143**, 1734–1787 (2014).
57. Adriaenssens, L. & Ballester, P. Hydrogen bonded supramolecular capsules with functionalized interiors: the controlled orientation of included guests. *Chem. Soc. Rev.* **42**, 3261–3277 (2013).
58. Shi, S. et al. Distinct reactivity differences of metal oxo and its corresponding hydroxo moieties in oxidations: implications from a manganese(IV) complex having dihydroxide ligand. *Angew. Chem. Int. Ed.* **50**, 7321–7324 (2011).

59. Gong, H.-Y. et al. Methylazacalixpyridines: remarkable bridging nitrogen-tuned conformations and cavities with unique recognition properties. *Chem. Eur. J.* **12**, 9262–9275 (2006).
60. Zhang, E.-X., Wang, D.-X., Zheng, Q.-Y. & Wang, M.-X. Synthesis of large macrocyclic azacalix[n]pyridines ($n = 6$–9) and their complexation with fullerenes C_{60} and C_{70}. *Org. Lett.* **10**, 2565–2568 (2008).
61. Frisch, M. J. et al. *Gaussian 09*, Revision D.01 (Gaussian, Inc., Wallingford, CT, 2013).
62. Becke, A. D. Density-functional thermochemistry. III. The role of exact exchange. *J. Chem. Phys.* **98**, 5648–5652 (1993).
63. Lee, C., Yang, W. & Parr, R. G. Development of the Colle-Salvetti correlation-energy formula into a functional of the electron density. *Phys. Rev. B* **37**, 785–789 (1988).
64. Dunning, T. H. J. Gaussian basis sets for use in correlated molecular calculations. I. The atoms boron through neon and hydrogen. *Chem. Phys.* **90**, 1007–1023 (1989).
65. Dunning, T. H. J. A road map for the calculation of molecular binding energies. *Phys. Chem. A* **104**, 9062–9080 (2000).
66. Hehre, W. J., Ditchfield, R. & Pople, J. A. Self-consistent molecular orbital methods. XII. Further extensions of Gaussian-type basis sets for use in molecular orbital studies of organic molecules. *J. Chem. Phys.* **56**, 2257–2261 (1972).
67. Wadt, W. R. & Hay, P. J. *Ab initio* effective core potentials for molecular calculations. Potentials for main group elements Na to Bi. *J. Chem. Phys.* **82**, 284–298 (1985).
68. Hay, P. J. & Wadt, W. R. *Ab initio* effective core potentials for molecular calculations. Potentials for the transition metal atoms Sc to Hg. *J. Chem. Phys.* **82**, 270–283 (1985).
69. Hay, P. J. & Wadt, W. R. *Ab initio* effective core potentials for molecular calculations. Potentials for K to Au including the outermost core orbitals. *J. Chem. Phys.* **82**, 299–310 (1985).
70. Dunning, T. H Jr., Hay, P. J. & Schaefer, H. F III. *Methods of Electronic Structure, Theory*. (Plenum Press: New York, 1977).

Acknowledgements

Financial support by NSFC (21772111, 21821001 and 21661132006) is gratefully acknowledged. We are grateful to Profs. Ming-Tian Zhang (Tsinghua University), Hai Xiao (Tsinghua University), Shang-Da Jiang (Peking University), Hao-Ling Sun (Beijing Normal University) and Dr. Li-Zhi Tao (UC Davis) for helpful discussion.

Author contributions

L.Z. conceived and supervised the project. The synthetic experiments and characterizations were carried out by S.Z. All authors discussed the results and commented on the manuscript.

Competing interests

The authors declare no competing interests.

Additional information

Supplementary information is available for this paper at https://doi.org/10.1038/s41467-019-12889-w.

Correspondence and requests for materials should be addressed to L.Z.

Peer review information *Nature Communications* thanks the anonymous reviewer(s) for their contribution to the peer review of this work.

Reprints and permission information is available at http://www.nature.com/reprints

Publisher's note Springer Nature remains neutral with regard to jurisdictional claims in published maps and institutional affiliations.

Open Access This article is licensed under a Creative Commons Attribution 4.0 International License, which permits use, sharing, adaptation, distribution and reproduction in any medium or format, as long as you give appropriate credit to the original author(s) and the source, provide a link to the Creative Commons license, and indicate if changes were made. The images or other third party material in this article are included in the article's Creative Commons license, unless indicated otherwise in a credit line to the material. If material is not included in the article's Creative Commons license and your intended use is not permitted by statutory regulation or exceeds the permitted use, you will need to obtain permission directly from the copyright holder. To view a copy of this license, visit http://creativecommons.org/licenses/by/4.0/.

© The Author(s) 2019